



Assessment of 2D/3D numerical modeling for deep dynamic stall experiments



A. Zanotti*, R. Nilifard, G. Gibertini, A. Guardone, G. Quaranta

Politecnico di Milano, Dipartimento di Scienze e Tecnologie Aeroespaziali, Campus Bovisa, Via La Masa 34, 20156 Milano, Italy

ARTICLE INFO

Article history:

Received 18 February 2013

Accepted 24 August 2014

Available online 22 September 2014

Keywords:

Dynamic stall

Oscillating airfoil

Wind tunnel

Computational fluid dynamics

ABSTRACT

The results of computational fluid dynamics (CFD) simulations in two and three spatial dimensions are compared to pressure measurements and particle image velocimetry (PIV) flow surveys to assess the suitability of numerical models for the simulation of deep dynamic stall experiments carried out on a pitching NACA 23012 airfoil. A sinusoidal pitching motion with a 10° amplitude and a reduced frequency of 0.1 is imposed around two different mean angles of attack of 10° and 15°. The comparison of the airloads curves and of the pressure distribution over the airfoil surface shows that a three-dimensional numerical model can better reproduce the flow structures and the airfoil performance for the deep dynamic stall regime. Also, the vortical structures observed by PIV in the flow field are better captured by the three-dimensional model. This feature highlighted the relevance of three-dimensional effects on the flow field in deep dynamic stall.

© 2014 Elsevier Ltd. All rights reserved.

1. Introduction

Several rotary-wing aircraft designs currently in advanced or preliminary development stage, such as the tiltrotor, like Bell Boeing V-22, AgustaWestland AW609 (Barbour, 2000) and ERICA concept (Gibertini et al., 2011), or the compound like Sikorsky X2, or the Eurocopter X3, are indeed revolutionary configurations which introduce significant changes with respect to standard helicopter designs. These new configurations were introduced to increase the maximum forward speed of the aircraft, which is currently limited by the occurrence of the dynamic stall on the retreating blade (McCroskey, 1981; Leishman, 2007).

The prediction of the onset and evolution of dynamic stall is a very challenging task. The research on dynamic stall is now focusing on the evaluation of reliable numerical tools for the simulation of this nonlinear, highly unsteady phenomenon, characterised by the rapid formation, migration and shedding of strong vortices (Visbal, 2011). In particular, three-dimensional effects in dynamic stall were recently studied by comparing two- and three-dimensional simulations (see for instance Spentzos et al., 2005; Martinat et al., 2008; Costes and Richez, ; Wang et al., 2012; Klein et al., 2012).

The verification of the numerical models requires thorough comparison between the simulations results and a comprehensive experimental data base (Coton and Galbraith, 1999; Raffel et al., 2011), in particular for the deep dynamic stall conditions. With this aim, a new experimental-numerical activity started at Politecnico di Milano. Wind tunnel tests were carried out on a pitching NACA 23012 blade section. The airfoil was selected since, being a typical helicopter blade airfoil, it was already employed by other researchers in experimental activities about the dynamic stall on pitching blade

* Corresponding author.

E-mail address: alex.zanotti@polimi.it (A. Zanotti).

Nomenclature		DSTA	Dipartimento di Scienze e Tecnologie Aerospaziali
α	angle of attack (deg)	DSV	Dynamic Stall vortex
α_m	mean angle of attack (deg)	f	oscillation frequency (Hz)
α_a	pitching oscillation amplitude (deg)	k	reduced frequency = $\pi f c / U_\infty$
Δx_{LE}	minimum streamwise grid spacing along airfoil at leading edge	M	Mach number
Δx_{TE}	minimum streamwise grid spacing along airfoil at trailing edge	N	number of grid points
Δx_s	maximum streamwise grid spacing along airfoil	N_{tot}	total number of grid points
Δz	spanwise grid spacing along blade section model	N_x	number of grid points along the airfoil surface
ω	circular frequency (rad/s)	N_y	number of grid points in the direction normal to the airfoil surface
b	blade section model span (m)	N_z	number of layers in boundary layer
c	blade section model chord (m)	PIV	Particle image velocimetry
C_L	lift coefficient	Re	Reynolds number
C_M	pitching moment coefficient about the airfoil quarter chord	TS	Time steps
C_p	pressure coefficient	U	streamwise velocity (m/s)
d	distance along the normal to chord direction (m)	$ U $	velocity magnitude (m/s)
		U_∞	free-stream velocity (m/s)
		x	chordwise coordinate axis
		y	normal coordinate axis
		z	spanwise coordinate axis

sections (Leishman, 1990; Raffel et al., 1995a). The experimental rig was designed to reproduce the deep dynamic stall condition for a full-scale helicopter rotor blade section. The experimental setup is suitable for different measurement techniques including unsteady pressure measurements, obtained from miniaturized pressure transducers installed on the midspan airfoil contour, and particle image velocimetry (PIV), which makes it possible to completely characterise the time-dependent flow field to achieve a detailed insight of the different stages of the dynamic stall process. The main goal of the research effort currently ongoing at Politecnico di Milano is to obtain reliable numerical models to be used in the development and sizing of new control devices for dynamic stall effect mitigation, to be tested in the same rig.

The wind tunnel tests of airfoils are affected by sidewall interference. In particular, when airfoil stall occurs, the flow rapidly becomes three-dimensional (Leishman, 1990), even in the case of a model spanning from wall to wall (Nishino and Shariff, 2010). A possible mitigation of this effect is the wall boundary layer suction (Catalano, 2004) but its implementation together with an oscillating airfoil system, although not impossible in principle, would be quite complex and, actually, the known reference experiments on airfoil dynamic stall (see for instance Gardner et al., 2011; Leishman, 1990; Carr et al., 1978; Raffel et al., 1995b) were carried out without suction.

In the present activity, both two and three-dimensional CFD models were created using EDGE (Eliasson, 2002), a compressible Navier-Stokes solver developed at FOI, the Swedish Defense Research Agency. Two- and three-dimensional numerical results were compared to the experimental ones to expose the suitability of the models to reproduce the performance and the flow physics involved in the deep dynamic stall regime.

In Section 2, the experimental setup is outlined. In Section 3, the EDGE code is briefly described and the two- and three-dimensional CFD models are detailed. Section 4 reports the comparison of two- and three-dimensional simulation against experimental results. Final considerations and comments are given in Section 5.

2. Experimental setup

Experimental activities were conducted at Politecnico di Milano in the low-speed closed-return wind tunnel of the Aerodynamics Laboratory of the DSTA. The wind tunnel has a rectangular test section with 1.5 m height and 1 m width. The maximum wind velocity is 55 m/s and the free stream turbulence level is less than 0.1%.

The airfoil model was manufactured in aluminum, with chord $c=0.3$ m and span $b=3.1$ c. The aspect ratio of the blade section model is close to that used for the models employed in the known reference experiments on dynamic stall (see for instance Gardner et al., 2011; Leishman, 1990). The model has an interchangeable midspan section for the different measurements techniques employed, one for PIV flow surveys and a second one for unsteady pressure measurement equipped with pressure taps positioned along the midspan chord line. The model is pivoted around two external steel shafts corresponding to the 25% of the airfoil chord.

The layout of the experimental rig designed for testing pitching airfoils is presented in Fig. 1. The model pitching motion is provided by a brushless servomotor with a 12:1 gear drive. Two different encoders mounted on the model external shaft mechanically decoupled from the motorized strut were used for feedback control and to get the instantaneous position of

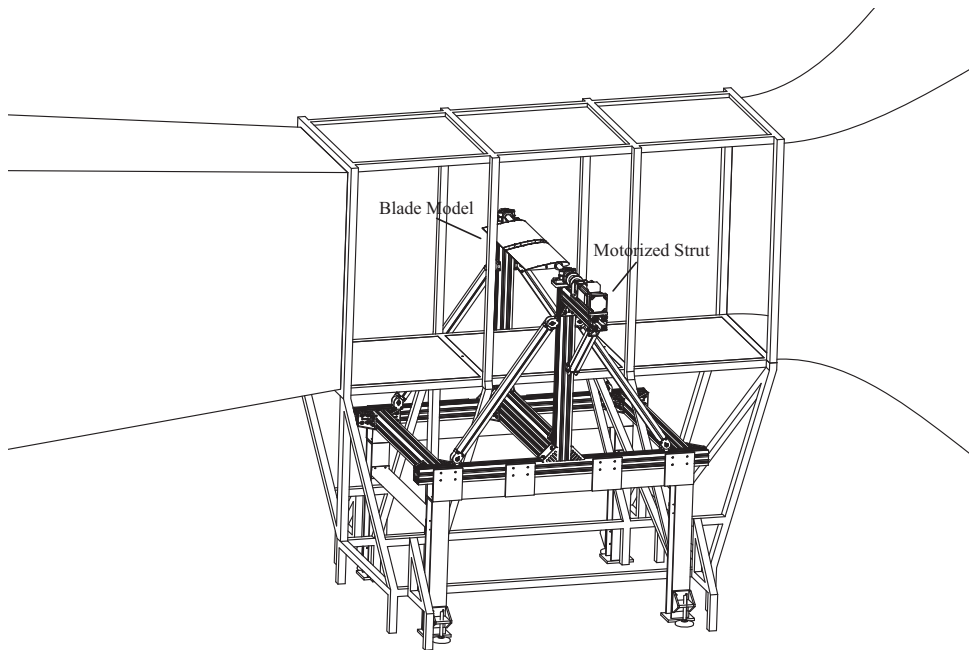


Fig. 1. Layout of the experimental rig for pitching airfoils.

the model during the tests. The model pitching motion is controlled by means of an ad hoc code implementing proportional and derivative control. More details about the pitching airfoil experimental rig can be found in Zanotti (2012) and Zanotti et al. (2011).

The two deep dynamic stall conditions tested consist in pitching cycles characterised by a mean angle of attack of $\alpha_m = 10^\circ$ and 15° , respectively, with constant oscillation amplitude of $\alpha_a = 10^\circ$ and reduced frequency of $k=0.1$. These conditions correspond to the deep dynamic stall regime as defined in McCroskey (1981), in which a portion of the upstroke is extended beyond the static stall angle. The pitching conditions were tested at relatively low speed (30 m/s) that is well within the test rig capabilities, corresponding to a Reynolds number of $Re=6 \times 10^5$ and a Mach number of $M = 0.09$. Such a low testing speed was chosen to avoid fatigue issues on the model strut due to the long run time required by the PIV measurements.

2.1. Unsteady pressure measurement setup

The time history of the lift and pitching moment during a pitching cycle was evaluated by the integration of the phase averaged pressures collected over 30 complete pitching cycles. The phase average of the pressure signals was computed using a bin of 0.1° angle of attack amplitude. The pressures were measured by means of 21 Kulite fast-response pressure transducers located inside the model interchangeable midspan section. The positions of the pressure taps around the model midspan airfoil contour are illustrated in the sketch of Fig. 2.

The pressure ports on the lower and upper surfaces of the airfoil closest to the trailing edge are located at 90% of the chord (similarly to the model used by Chandrasekhara et al., 2008) since installation closer to the trailing edge was not feasible due to insufficient model thickness. Two second order polynomial functions interpolating the last three pressure ports signals, respectively, on the upper and lower surface of the airfoil, were considered to extrapolate the airfoil trailing edge pressure that is needed to compute the chord-wise integral of the airloads. In particular the pressure at the trailing edge was computed as the average of those extrapolated at the airfoil trailing edge position, see Chandrasekhara et al. (2008). An estimation of the uncertainty due to the limited number of pressure sensors was carried out on the base of steady state simulations (using XFOIL code by Drela and Youngren, 2001), showing a maximum discretisation error in the lift and pitching moment coefficients respectively, of 0.027 and 0.003 for $\alpha < 10^\circ$. When boundary layer separation is present unsteady pressure disturbances are expected. Thus a certain degree of uncertainty related to the lack of the local pressure information at the trailing edge is present and difficult to be quantified precisely. Nevertheless, the regular behaviour of the pressure up to 90% of the chord allowed to assume that remarkable errors are not included in the evaluation of the global pitching moment coefficients.

2.2. Particle image velocimetry setup

The PIV system used a double shutter CCD camera with a 12 bit, 1280×1024 pixel array and a 55 mm lens. The measurement area covers the whole airfoil upper surface and was composed by four $103 \text{ mm} \times 82 \text{ mm}$ measurement

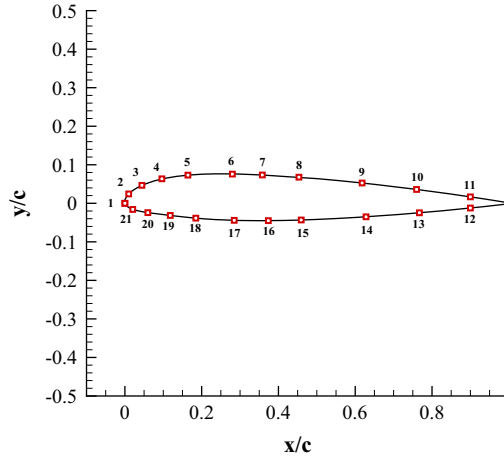


Fig. 2. Pressure taps location on the NACA 23012 model midspan section.

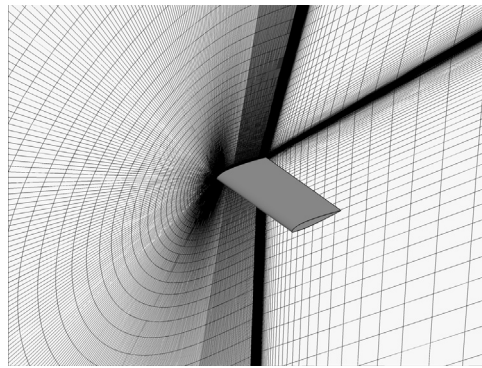


Fig. 3. Three-dimensional grid. The baseline C-type grid is illustrated on the symmetry plane.

windows spanning the chord direction, with a small overlapping between adjacent windows. The choice to compose the complete observation field with smaller measurement windows was dictated by the need to obtain image pairs with better resolution.

A Nd:Yag double pulsed laser, with 200 mJ output energy and wavelength 532 nm, was positioned over the top of the test section to illuminate the observation area through a slot in the wind tunnel roof.

The image pairs post-processing was carried out by means of the PIVview 2C/3C software of PIVTEC. Multigrid technique ([Raffel et al., 1998](#)) was employed to correlate the image pairs, starting from an interrogation window of 96×96 pixels to a window of 32×32 pixels. In order to filter out the effect of turbulent oscillations, the velocity flow fields were phase averaged over 40 image pairs.

Additional details on the measurement techniques setup can be found in [Zanotti et al. \(2011\)](#) and [Zanotti \(2012\)](#).

3. Numerical modeling of dynamic stall

The CFD solver used for this study is the EDGE code developed by FOI, the Swedish Defense Research Agency ([Eliasson, 2002](#)). The code is capable of solving flows with different regimes from inviscid to fully turbulent using various turbulence models. RANS (Reynolds-Averaged Navier–Stokes), DES (Detached-Eddy Simulation) and LES (Large Eddy simulation) models in 2/3 dimensions are implemented.

For numerical simulations in two spatial dimensions, a 2D C-type grid was used (see [Fig. 3](#)). The dimensionless wall distance y^+ of the first grid point in the normal direction is less than one, which corresponds to a distance of about $10^{-5} c$. A non-reflecting far-field boundary is located at $20 c$ away from the airfoil. The errors due to the choice of the far-field distance should not influence the main conclusions of the present work ([Richter et al., 2011](#)), as suggested by the results of the study by [Desterac \(2011\)](#) for fixed-wing aircraft applications. Three 2D grids with different cell densities were considered in order to study the grid sensitivity of the numerical solutions, namely G1, G2 and G3. The grid details are shown in [Table 1](#).

Table 1

Detailed information of different 2D grids employed.

Grid ID	N_{tot}	N_x	N_y	N_L	Δx_{LE}	Δx_{TE}	Δx_s
G1	108 380	660	130	40	0.0022	0.001249	0.0072
G2	318 000	1500	190	60	0.00088	0.00062	0.0036
G3	615 000	2500	250	60	0.00056	0.00046	0.0024

The 3D grids were built by extruding the baseline 2D grid G1 for 1.5 c in the spanwise direction ($b/c=1.5$) with a uniform Δz spacing of about 0.05 ($N_z=30$) and 0.025 ($N_z=60$). The 3D grids with a total number of 3 251 400 and 6 502 800 elements are denoted as G4 and G5. The computational domain was decomposed into 36 subdomains that were distributed among processors using MPI technique.

The URANS simulations were carried out using the Hellsten $k-\omega$ turbulence model calibrated using the EARSM (Explicit Algebraic Reynolds Stress Model) assumption by Wallin and Johansson to define the relation between Reynolds stresses and strain rate tensor (Wallin, 2003; Hellsten, 2005). The dynamic viscosity is kept constant because the temperature differences are small within the flowfield. A central scheme plus a Jameson type diffusion is used for the spatial discretization of the advection term. The second order dissipation coefficient is $\text{vis}_{\parallel}=0.8$ and the fourth order dissipation one is $\nu_{\text{IV}}=0.05$. The values of these parameters were chosen to obtain a good numerical accuracy for the problem under scrutiny.

In the present activity, it was decided to investigate the effect of three-dimensional structures on the deep dynamic stall by running a 3D numerical simulation of the model blade section. Differently from other authors that carried out simulations resolving all geometrical details of the wind tunnel walls and boundary layers (Klein et al., 2012), the scope of this work was to highlight the importance of the intrinsic three-dimensional effects of the deep dynamic stall, which do not depend from the wind tunnel, and how much they impact on the results. Therefore, a no-slip adiabatic condition was imposed along the airfoil surface and a slip condition was imposed on both side boundaries of the 3D grid to obtain a solution as much as possible independent from the geometry of the wind tunnel. In this way, a numerical model that keep the computational burden at an acceptable level was obtained.

A characteristic boundary condition was also prescribed at the far-field boundary. In all computations, a sinusoidal pitching motion is imposed on the whole grid which moves as a rigid body. The numerical results were extracted after four full cycles to ensure a periodic state. In the multigrid technique, a simplified form of the artificial dissipation operator based on second order differences was used to save computational time and to increase the numerical damping. The coefficient of the simplified artificial dissipation term is $\nu_z=0.15$.

4. Results and discussion

4.1. Grid dependence and time step dependence studies

A time-step dependence assessment for the two-dimensional simulations over G1 and G2 grids is reported in Figs. 4 and 5, respectively, considering the test condition with $\alpha_m=10^\circ$. In Fig. 4, the lift and pitching moment coefficient histories computed using G1 grid with different time steps (TS) per period are compared to the experimental data. The numerical lift and pitching moment coefficients curves overlap for the whole upstroke phase, when the flow field is attached to the airfoil surface, as well as at the start and in the last part of the downstroke motion, where the flow reattachment occurs. In the first portion of the downstroke phase (approximately between $\alpha=20^\circ$ and $\alpha=10^\circ$), characterised by a significant flow separation and a high degree of unsteadiness, the curves presents small discrepancies. A limited difference also remains in the absolute C_M peak computed for the simulations with time resolution between 204 and 816 time-steps. Nevertheless, the discrepancies observed for the C_L curves computed with time resolution between 204 and 816 time-steps are also small in this phase of the motion and are comparable to the ones observed in the work by Wang et al. (2012), where the solution was considered converged. Thus, 720 time steps per period were considered sufficient to represent the dynamics of the stall and to assure that the flow structures are correctly captured, even if the solution cannot be considered almost independent from time-steps. Similar considerations can be deduced from the comparison of the airloads curves computed for the finer grid G2, see Fig. 5.

In Fig. 6 2D simulations results obtained with 720 time steps per period are presented for three different grid resolutions. Similarly to what observed in the time-step dependence study, the lift coefficient curves computed with the different grids are overlapped for the whole upstroke motion and in the first and last portion of the downstroke. In the first half of the downstroke motion the lift curves obtained over G2 and G3 show contained differences. In particular, the results over C_L are similar to the ones obtained in the grid dependence studies reported in the works by Richter et al. (2011) and Wang et al. (2012). Nevertheless, even if it cannot be considered almost grid independent, the solution obtained over G2 grid can be considered acceptable.

The same resolution in space and time was used for the 2D simulations of the test case with $\alpha_m=15^\circ$ as similar conclusions can be deduced from the time-step and grid dependence studies reported in Nilifard (2013).

Considering now the three-dimensional case, Fig. 7 shows the lift and pitching moment coefficients curves computed using G4 grid for five different values of the time steps. For the 3D simulations the lift and pitching moment coefficients

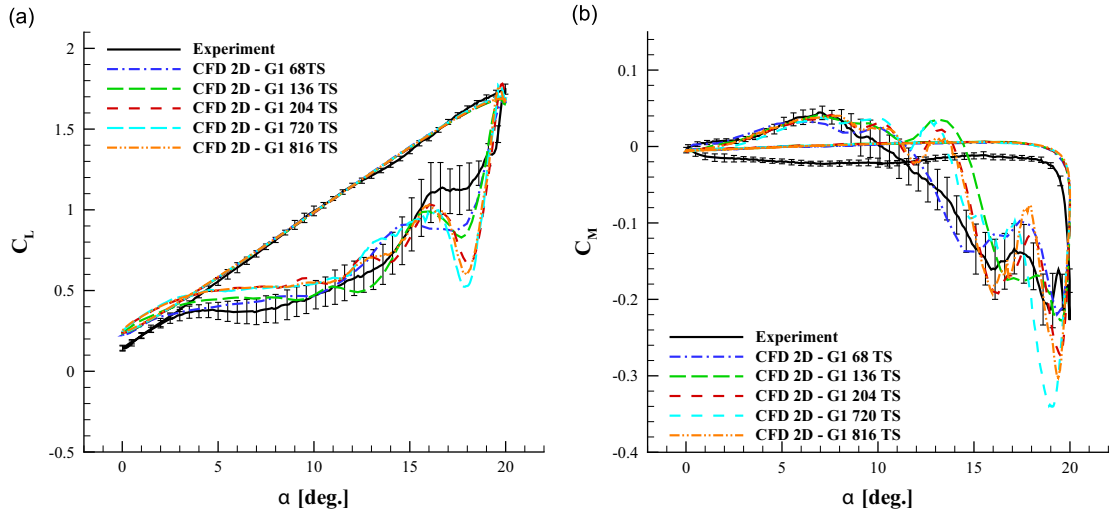


Fig. 4. Comparison of experimental and numerical C_L and C_M computed for 2D model over G1 with various time steps: $\alpha = 10^\circ + 10^\circ \sin(\omega t)$, $k=0.1$ ($Re=6 \times 10^5$ and $M=0.09$).

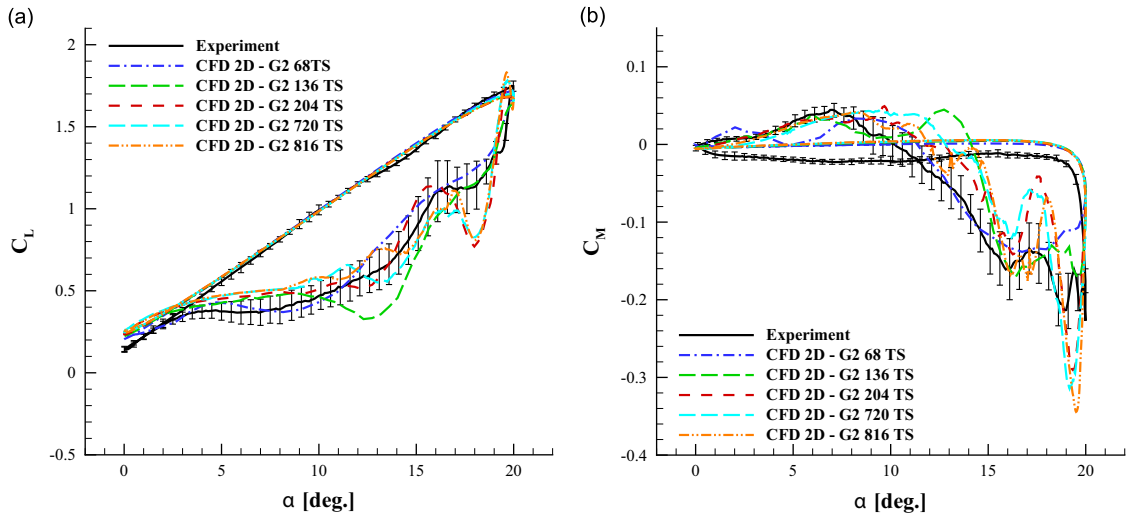


Fig. 5. Comparison of experimental and numerical C_L and C_M computed for 2D model over G2 with various time steps: $\alpha = 10^\circ + 10^\circ \sin(\omega t)$, $k=0.1$ ($Re=6 \times 10^5$ and $M=0.09$).

were computed by the integration of pressure evaluated in the model central section. Analogously to the 2D case, a very good convergence in time is obtained during upstroke. In downstroke, the lift and pitching moment coefficients curves computed with 720 and 1440 time-steps show small discrepancies in the range $18^\circ < \alpha < 12^\circ$ that is characterised by the fast passage of strong vortical structures. Therefore, the results obtained with 720 time steps over the G4 grid are presented, since the accuracy of the results can be considered acceptable.

As it was stated in the work by Klein et al. (2012), the spatial convergence of 3D simulations results for the fully stalled flow typical of the deep dynamic stall regime represents a very demanding task due to the high computational cost. Therefore, the limited computational resources available for this activity did not allow a grid dependence study with 720 time steps. A tentative grid dependence assessment is presented in Fig. 8 with 68 TS assuming that time error is decoupled from space error. Under this hypothesis, the small discrepancies observed between the C_L curves that are limited to the downstroke portion give the qualitative indication that there is not a strong grid dependency for the 3D simulations. Nevertheless, taking also into account the comparison with experimental data, the solution obtained over G4 with 720 time steps can be considered a good compromise between accuracy and computational time. This is why this solution was analysed in the following.

Therefore, in order to show a consistent comparison between 2D and 3D numerical models, the results over G4 are first compared to the ones obtained from the 2D simulations carried out over G1, that was used as baseline mesh to build G4,

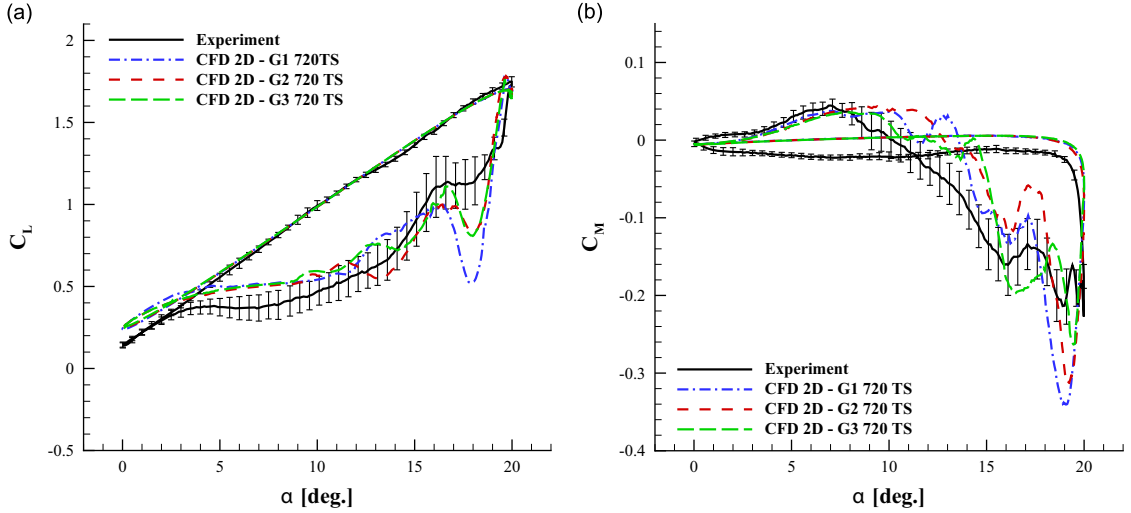


Fig. 6. Comparison of experimental and numerical C_L and C_M computed for 2D model with different grids: $\alpha = 10^\circ + 10^\circ \sin(\omega t)$, $k=0.1$ ($Re=6 \times 10^5$ and $M=0.09$).

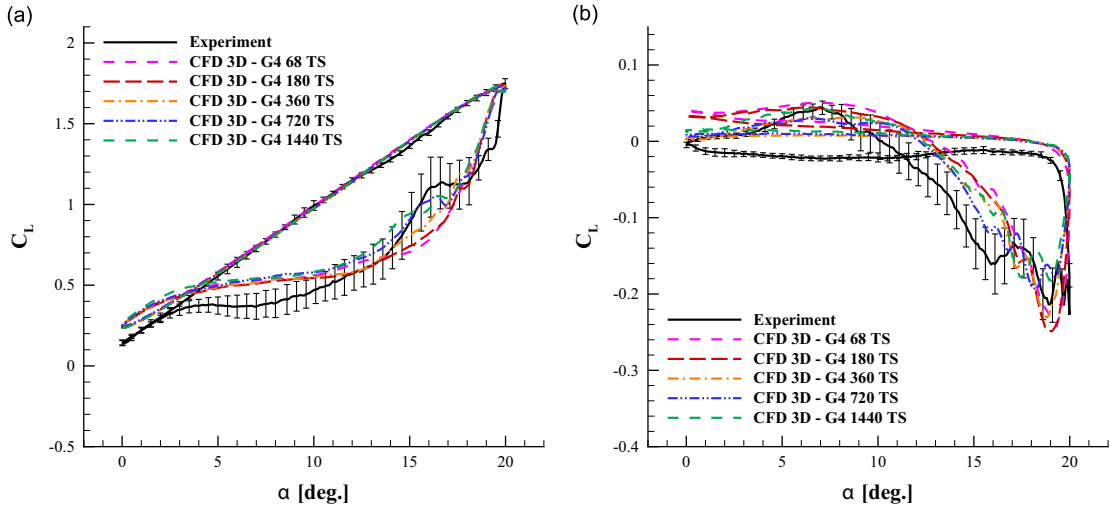


Fig. 7. Comparison of experimental and numerical C_L and C_M computed for 3D model with various time steps: $\alpha = 10^\circ + 10^\circ \sin(\omega t)$, $k=0.1$ ($Re=6 \times 10^5$ and $M=0.09$).

with the same resolution in time (720 TS). The results for the 2D simulations over G2 were also added in the following comparison to get further insight about the behaviour of the two-dimensional representation obtained over the finer grid.

4.2. Analysis of airloads

[Fig. 9](#) presents the comparison between the measured lift and quarter chord moment coefficients against the results of 2D and 3D simulations for the test condition with $\alpha_m=10^\circ$. Comparison of the pressure coefficient distribution for four angles of attack of interest is shown in [Fig. 10](#). The standard deviation of the airloads and pressure coefficients are plotted on the experimental curves. For 3D simulations the C_p are evaluated on the airfoil midspan contour.

The airloads comparison shows some discrepancies between numerical results and wind tunnel data. During the upstroke motion, the lift coefficient curves evaluated by both the 2D and 3D simulations are close to the experimental one, see [Fig. 9\(a\)](#). A fair agreement between the experimental and numerical C_p distribution can be observed for both 2D and 3D simulations at $\alpha=18^\circ$ during upstroke, see [Fig. 10\(a\)](#). On the other hand, for $\alpha=20^\circ$, the numerical models correctly capture the C_p distribution on the airfoil lower surface only, while discrepancies can be observed on the airfoil upper surface distributions (see [Fig. 10\(b\)](#)). In particular, the C_p distribution obtained for the 2D simulations over the different considered grids does not show significant differences for these test conditions.

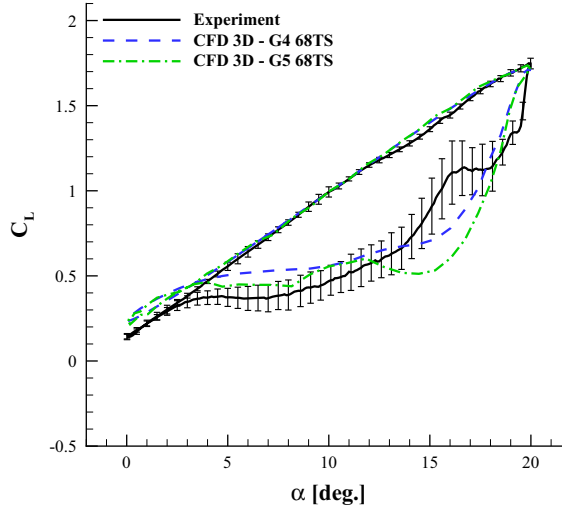


Fig. 8. Comparison of experimental and numerical C_L computed for 3D model with different grids: $\alpha = 10^\circ + 10^\circ \sin(\omega t)$, $k=0.1$ ($Re=6 \times 10^5$ and $M=0.09$).

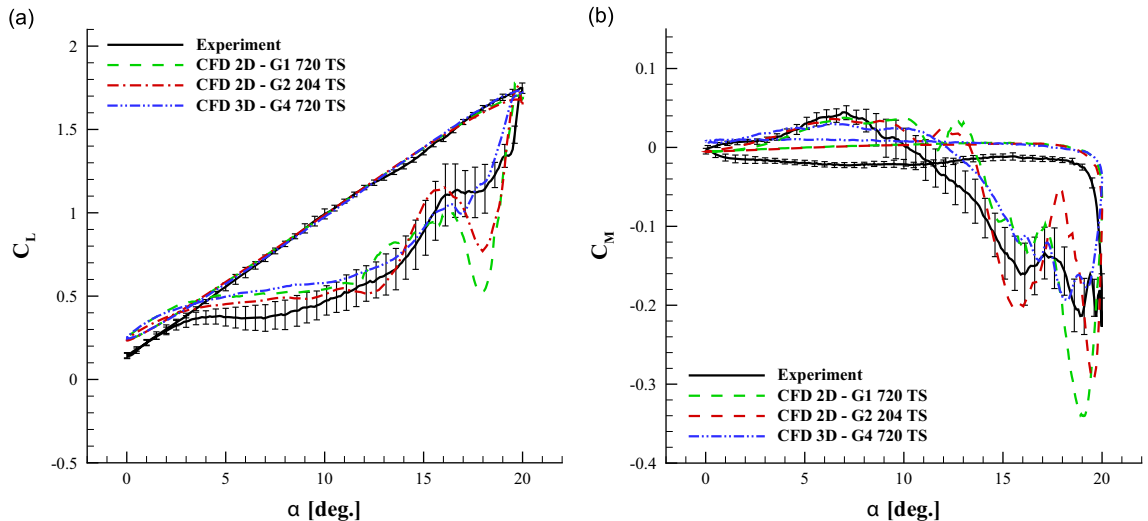


Fig. 9. Comparison of experimental and numerical airloads: $\alpha = 10^\circ + 10^\circ \sin(\omega t)$, $k=0.1$ ($Re=6 \times 10^5$ and $M=0.09$).

During the downstroke motion the flow field is characterised by the formation of strong vortices moving on the airfoil upper surface that produce large variations in the airloads. The 2D numerical models show more conspicuous oscillations of the lift and pitching moment curves with respect to the experimental data, in particular higher for the coarser grid G1. On the other hand, the 3D numerical model reproduces better both the oscillations and the hysteresis. In fact, the massive flow separation occurring in this part of the motion is three-dimensional and consequently the 2D model representation of the flow is inadequate to reproduce the spanwise development of the vortical structures. Therefore, similarly to what observed by Joubert et al. (2013), the above may explain the reproduction of stronger vortices in the 2D representation and the consequent higher peaks and oscillations of the airloads with respect to the 3D model and experimental data. In addition, the experimental peak value of the pitching moment coefficient is closer to the one obtained with the 3D simulation as well as the behaviour of the curve during the downstroke phase of the motion, see Fig. 9(b). Further insight in the airloads can be achieved from the C_p distribution comparison at $\alpha = 18^\circ$ and $\alpha = 16^\circ$ in downstroke. Indeed, as it can be observed from Fig. 10(c) and (d), the numerical models show an attached flow at the airfoil leading edge with a higher suction peak for the 2D numerical models. The experimental C_p distributions over the airfoil upper surface are not reproduced by either numerical models, showing a different separation point downstream the leading edge. However, a better agreement with the experimental data can be observed with the 3D model results on the airfoil lower surface.

Figs. 11 and 12 present the airloads and C_p distribution comparisons for the test condition with $\alpha_m = 15^\circ$. In this test case, a good agreement between numerical and experimental lift curve can be observed during the upstroke phase of the motion before the stall onset. A delay of the non-linear increase in slope due to the formation and migration of the dynamic stall

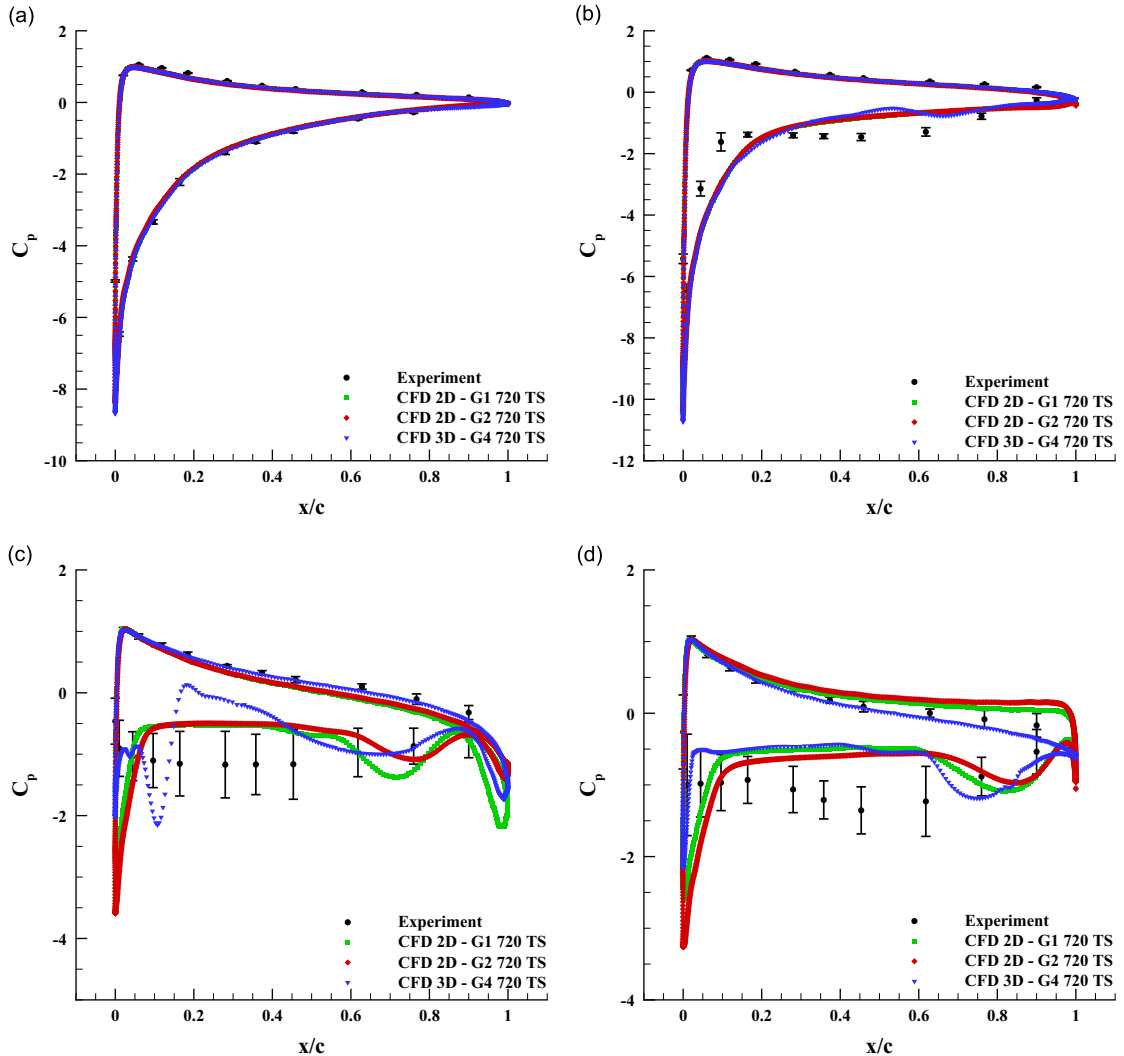


Fig. 10. Comparison between experiments and CFD for pressure coefficient distribution: $\alpha = 10^\circ + 10^\circ \sin(\omega t)$, $k=0.1$ ($Re=6 \times 10^5$ and $M=0.09$). (a) $\alpha = 18^\circ$ upstroke, (b) $\alpha = 20^\circ$ upstroke, (c) $\alpha = 18^\circ$ downstroke and (d) $\alpha = 16^\circ$ downstroke.

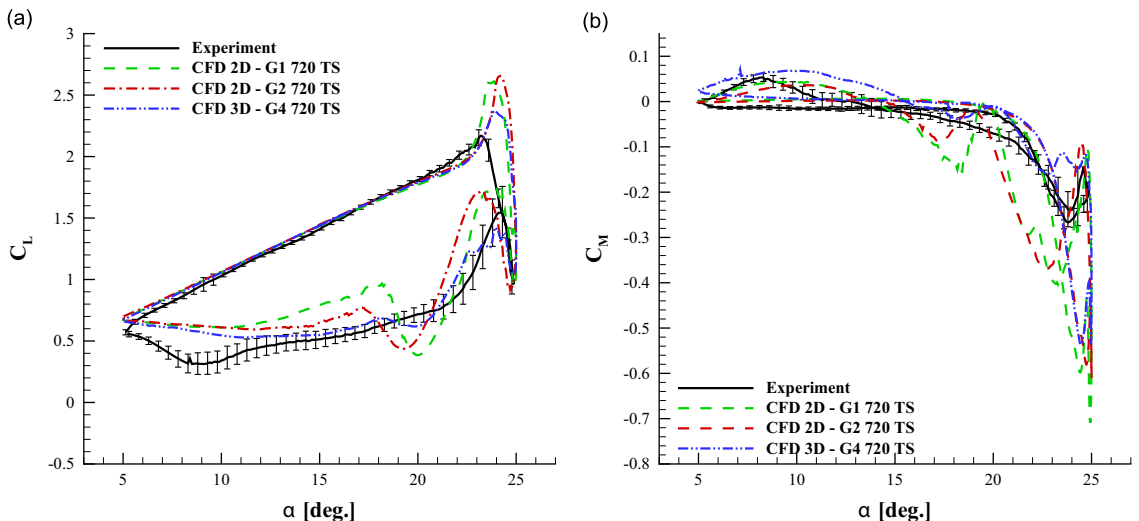


Fig. 11. Comparison of experimental and numerical airloads: $\alpha = 15^\circ + 10^\circ \sin(\omega t)$, $k=0.1$ ($Re=6 \times 10^5$ and $M=0.09$).

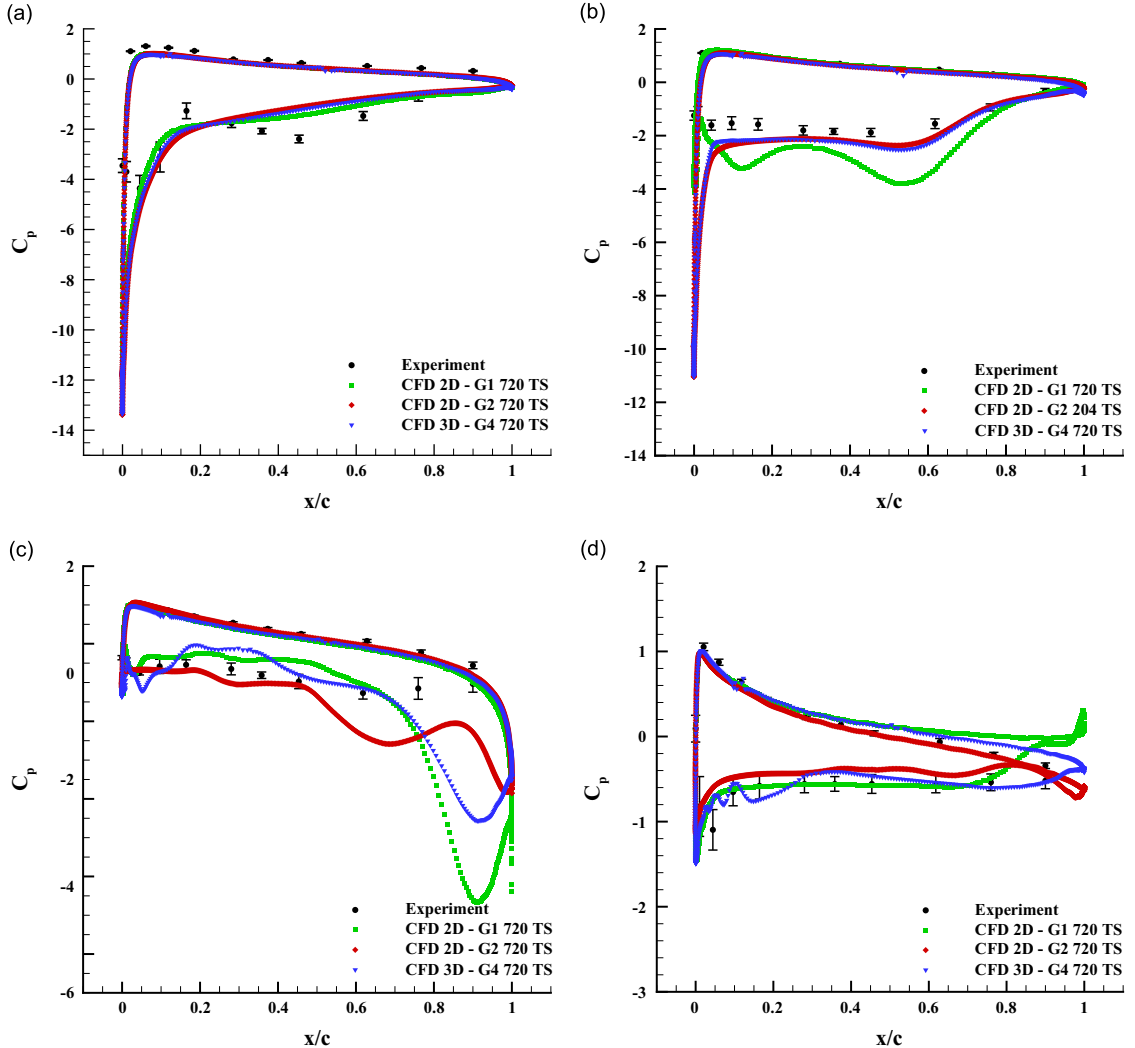


Fig. 12. Comparison between experiments and CFD for pressure coefficient distribution: $\alpha = 15^\circ + 10^\circ \sin(\omega t)$, $k=0.1$ ($Re=6 \times 10^5$ and $M=0.09$). (a) $\alpha = 23^\circ$ upstroke, (b) $\alpha = 24^\circ$ upstroke, (c) $\alpha = 25^\circ$ upstroke, and (d) $\alpha = 18^\circ$ downstroke.

vortex (DSV) with respect to the measurements was observed from the numerical curves obtained over 3D and 2D models over G2, while a fair agreement is observed for the 2D model over G1 grid, see Fig. 11(a). However, all the considered numerical models fail to capture the peak value of the lift coefficient, analogously to the results obtained by Klein et al. (2012). It can be assumed, following the indications of the results by Richter et al. (2011), that for such low Mach numbers test cases boundary layer transition may possibly influence the stall onset. In the present work, the influence of boundary layer transition was not investigated and only fully turbulent simulations were carried out. This assumption possibly explains the discrepancies observed with the experimental data in this phase of the motion characterised by complicated flow structures. Nevertheless, an overall better representation concerning the airfoil performance is achieved by using the 3D numerical model, which shows a closer agreement with experiments of the lift peak and of the lift breakdown at stall obtained by 3D simulation results with respect to the 2D ones.

Further insight about the numerical model behaviour can be obtained from the C_p comparison in the last part of the upstroke motion. At $\alpha = 23^\circ$ the numerical models predict an attached flow at the airfoil leading edge with a similar value of the suction peak, see Fig. 12(a). At $\alpha = 24^\circ$ in upstroke, similar features with respect to the previous test case are observed for the 3D and 2D numerical models over G2 grid. On the other hand, the C_p distribution on the upper surface obtained for the 2D model over G1 grid shows a quite different behaviour characterised by a drop of the suction peak value. In general, for these test conditions the experimental C_p distribution is well captured by the numerical models just on the airfoil lower surface. At the top of the upstroke motion ($\alpha = 25^\circ$) the experimental C_p distribution over the airfoil upper surface presents remarkable discrepancies with respect to the one computed by both numerical models, in particular in the trailing edge region. Thus, the comparison of the C_p distribution explains the significant overestimation of the computed pitching moment peak with respect to the measured value, analogously to what it was found in the works by Klein et al. (2012) and

[Wang et al. \(2012\)](#). In general, it is the authors's opinion that these discrepancies result from a different position of the separation point as predicted by the numerical models.

During the downstroke motion, the amplitude of the lift coefficient hump observed in the experimental curve is well captured only by the 3D numerical model. The 2D simulations results over G2 grid show a delay of this hump with respect

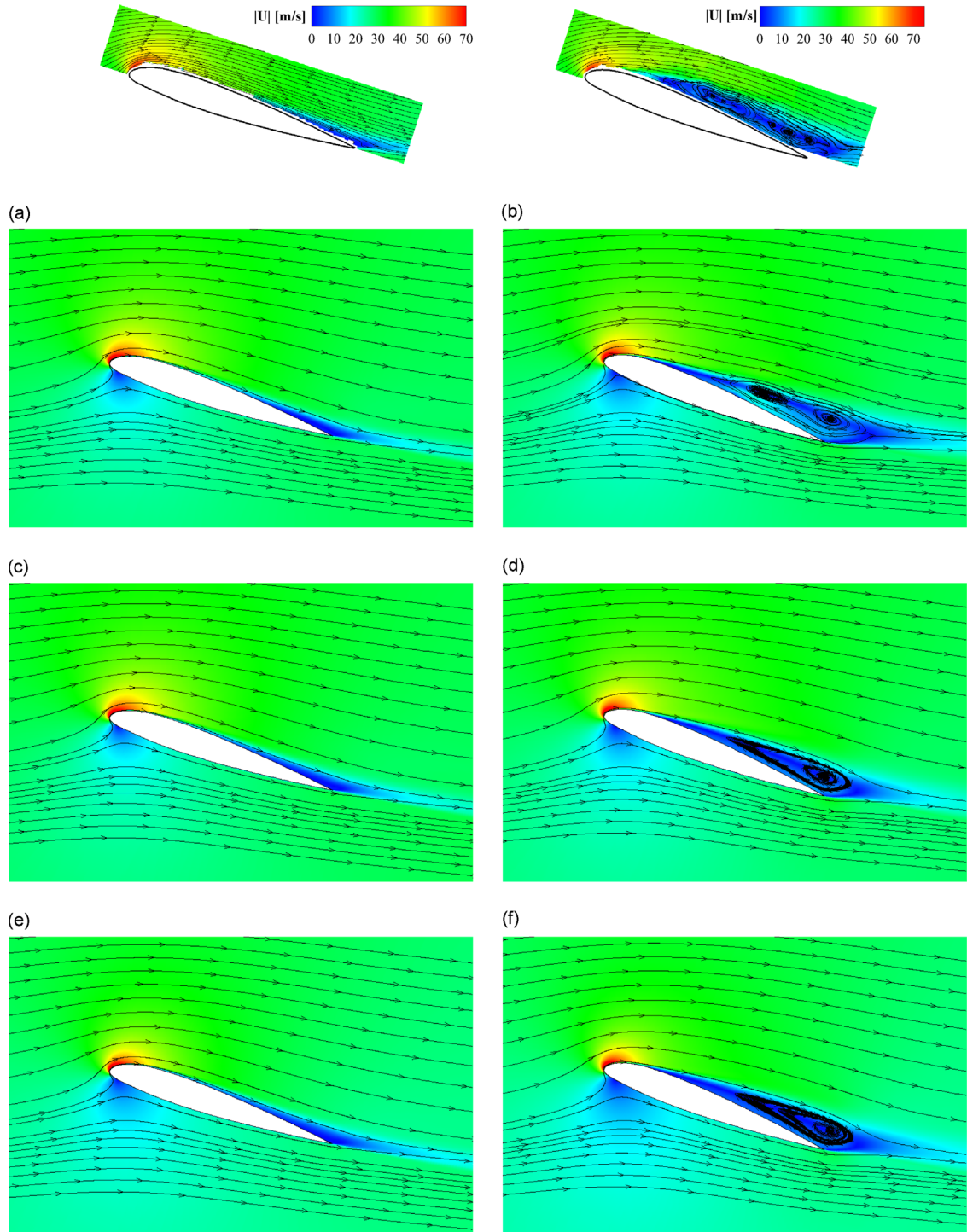


Fig. 13. Flow field comparison between experiments and CFD: streamlines superimposed on color maps of the velocity magnitude for $\alpha = 10^\circ + 10^\circ \sin(\omega t)$, $k=0.1$ ($Re=6 \times 10^5$ and $M=0.09$). (a) $\alpha = 18^\circ$ upstroke, experiment, (b) $\alpha = 20^\circ$ upstroke, experiment, (c) $\alpha = 18^\circ$ upstroke, CFD 3D – G4 720 TS, (d) $\alpha = 20^\circ$ upstroke, CFD 3D – G4 720 TS, (e) $\alpha = 18^\circ$ upstroke, CFD 2D – G1 720 TS, (f) $\alpha = 20^\circ$ upstroke, CFD 2D – G1 720 TS, (g) $\alpha = 18^\circ$ upstroke, CFD 2D – G2 204 TS and (h) $\alpha = 20^\circ$ upstroke, CFD 2D – G2 204 TS.

to the experiment that is not observed from the results over G1 grid. In particular, at $\alpha = 18^\circ$ in downstroke the numerical models capture fairly the experimental C_p distribution. Nevertheless, not negligible discrepancies can be observed at the trailing edge region for both the 2D numerical models, see Fig. 12(d).

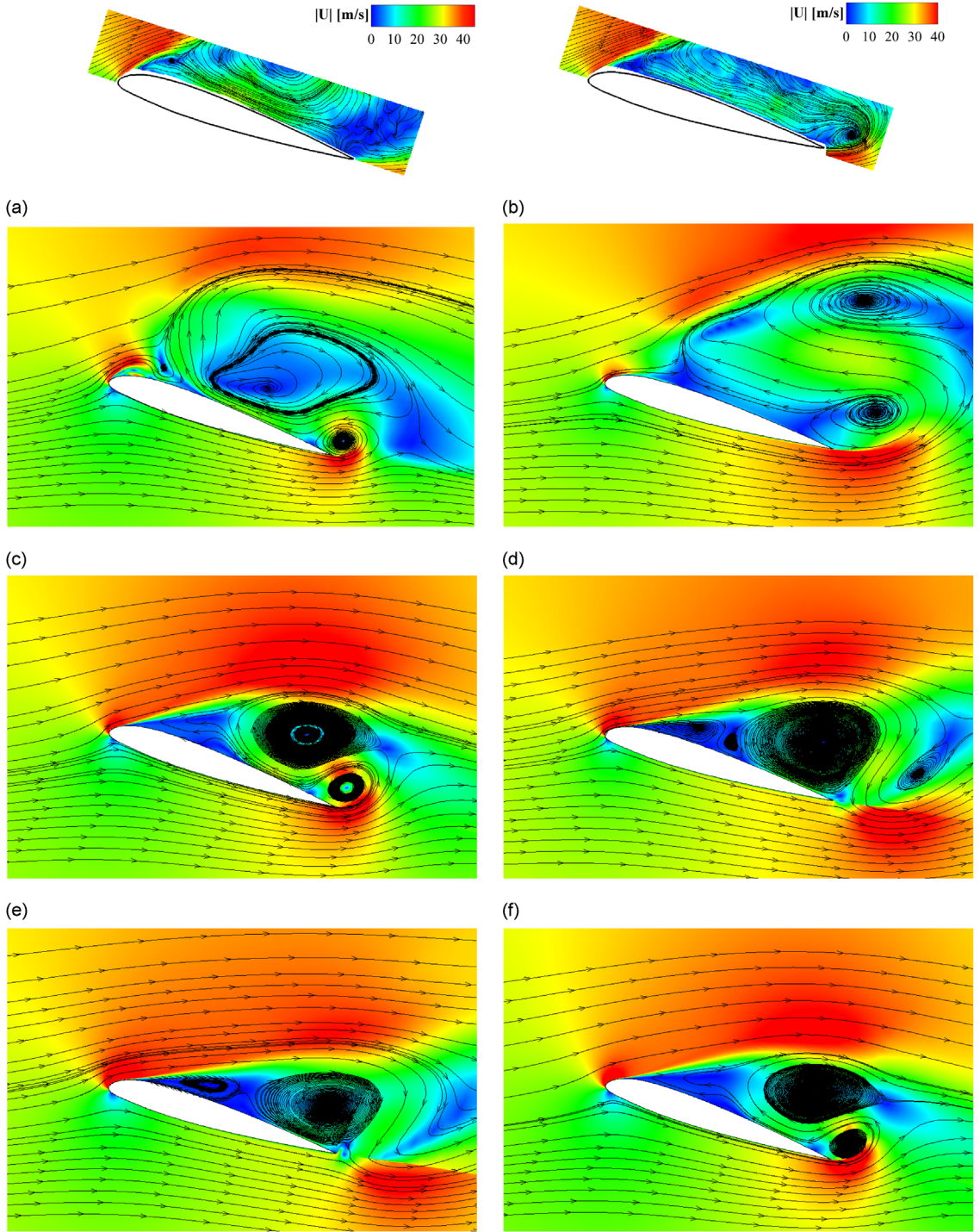


Fig. 14. Flow field comparison between experiments and CFD: streamlines superimposed on color maps of the velocity magnitude for $\alpha = 10^\circ + 10^\circ \sin(\omega t)$, $k=0.1$ ($Re=6 \times 10^5$ and $M=0.09$, continued). (a) $\alpha=18^\circ$ downstroke, experiment, (b) $\alpha=16^\circ$ downstroke, experiment, (c) $\alpha=18^\circ$ downstroke, CFD 3D – G4 720 TS, (d) $\alpha=16^\circ$ downstroke, CFD 3D – G4 720 TS, (e) $\alpha=18^\circ$ downstroke, CFD 2D – G1 720 TS, (f) $\alpha=16^\circ$ downstroke, CFD 2D – G1 720 TS, (g) $\alpha=18^\circ$ downstroke, CFD 2D – G2 204 TS and (h) $\alpha=16^\circ$ downstroke, CFD 2D – G2 204 TS.

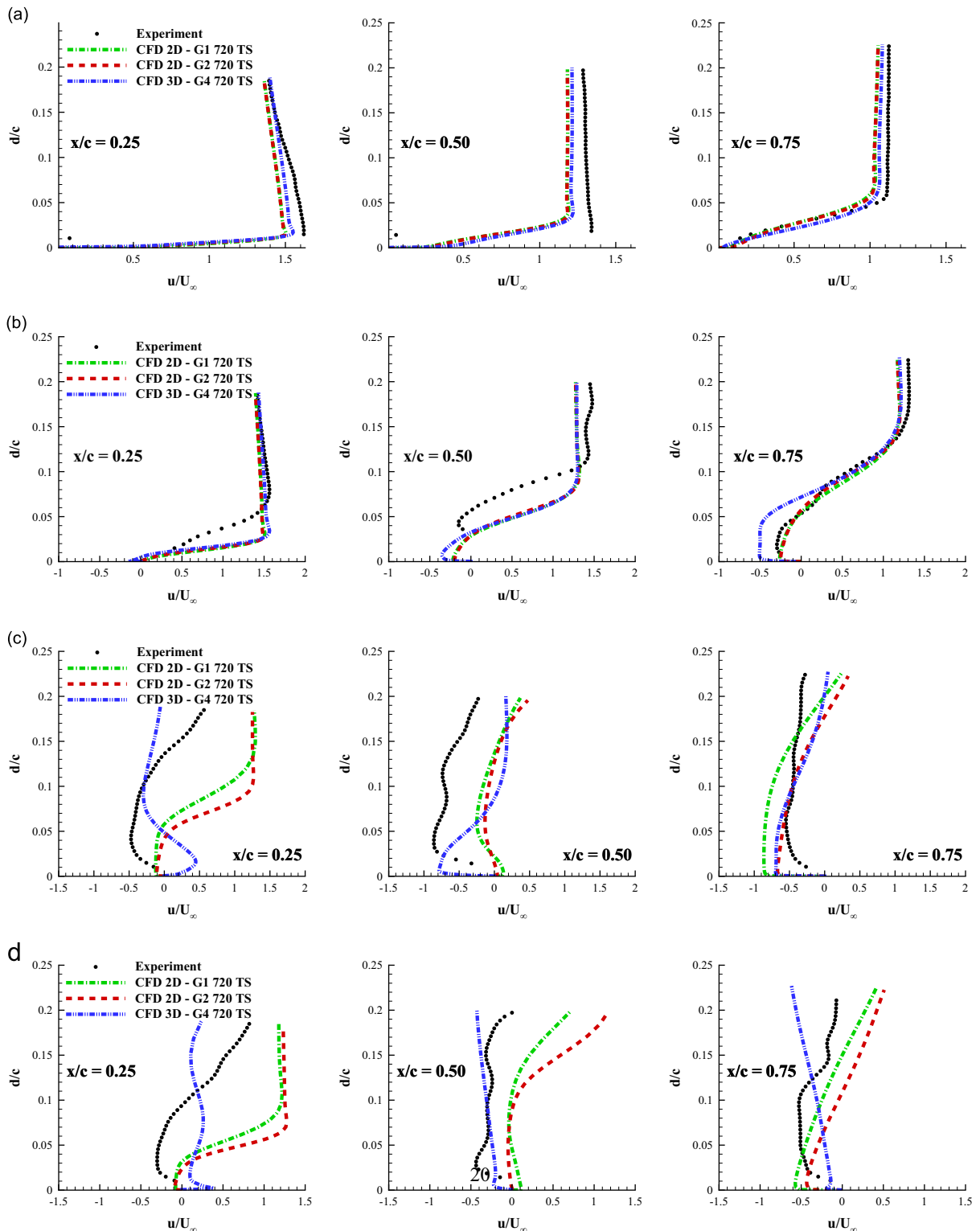


Fig. 15. Comparison between experiments and CFD for streamwise velocity profiles: $\alpha = 10^\circ + 10^\circ \sin(\omega t)$, $k=0.1$ ($Re=6 \times 10^5$ and $M=0.09$). (a) $\alpha = 18^\circ$ upstroke, (b) $\alpha = 20^\circ$ upstroke, (c) $\alpha = 18^\circ$ downstroke and (d) $\alpha = 16^\circ$ downstroke.

4.3. Analysis of flow field

The PIV results at wind tunnel model midspan (Zanotti and Gibertini, 2013) were compared to the velocity fields obtained by the 2D and 3D simulations. The phase-averaged velocity fields are shown by means of instantaneous

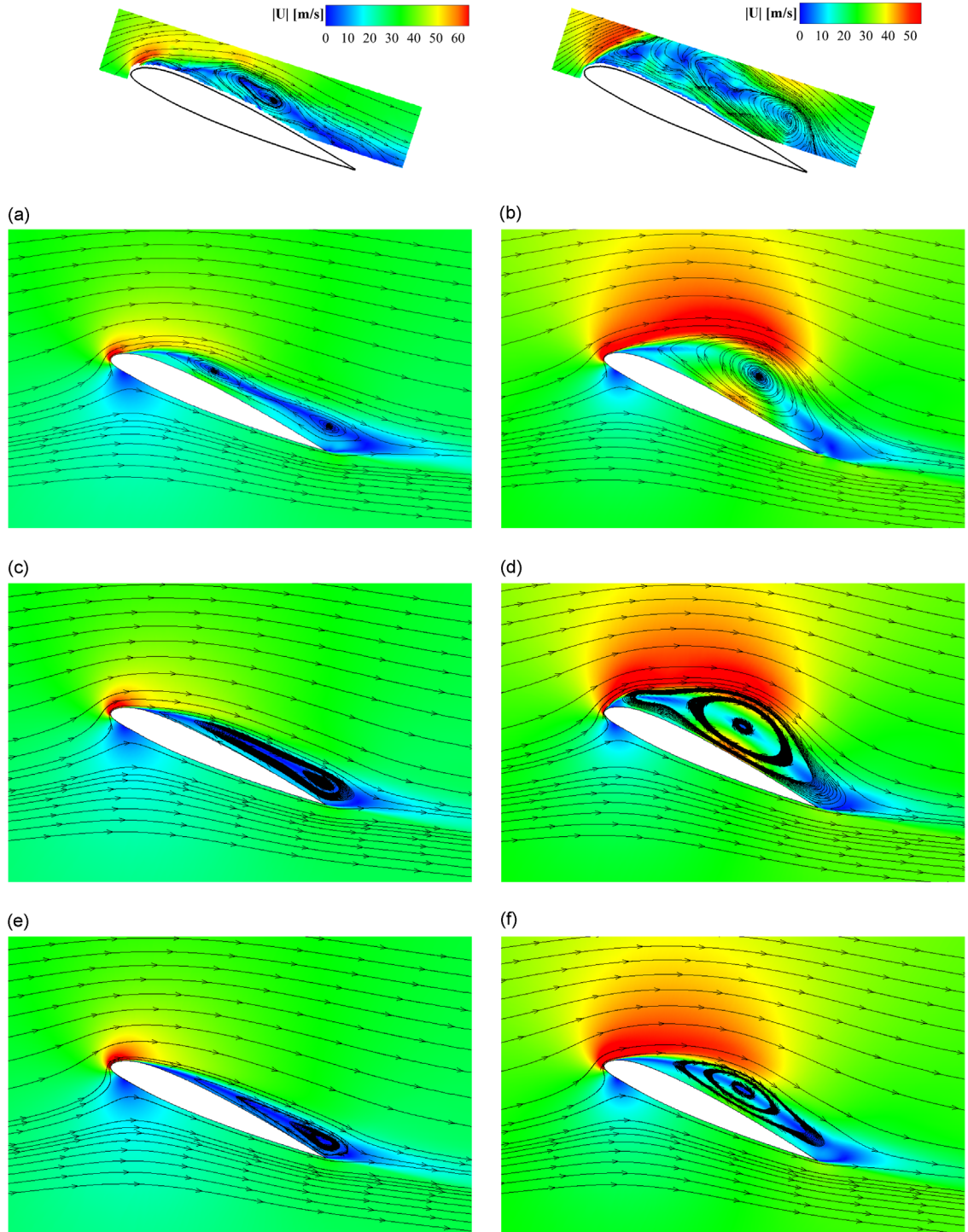


Fig. 16. Flow field comparison between experiments and CFD: streamlines superimposed on color maps of the velocity magnitude for $\alpha = 15^\circ + 10^\circ \sin(\omega t)$, $k=0.1$ ($Re=6 \times 10^5$ and $M=0.09$). (a) $\alpha = 23^\circ$ upstroke, experiment, (b) $\alpha = 24^\circ$ upstroke, experiment, (c) $\alpha = 23^\circ$ upstroke, CFD 3D – G4 720 TS, (d) $\alpha = 24^\circ$ upstroke, CFD 3D – G4 720 TS, (e) $\alpha = 23^\circ$ upstroke, CFD 2D – G1 720 TS, (f) $\alpha = 24^\circ$ upstroke, CFD 2D – G1 720 TS, (g) $\alpha = 23^\circ$ upstroke, CFD 2D – G2 720 TS and (h) $\alpha = 24^\circ$ upstroke, CFD 2D – G2 720 TS. (For interpretation of the references to color in this figure caption, the reader is referred to the web version of this article.)

streamlines patterns superimposed on color maps of velocity magnitude; the illustrated 3D numerical flow field is evaluated at midspan. The comparisons between the experimental and numerical flow field at the same four angles of attack of interest selected for C_p distribution comparison are shown in the Figs. 13–17. Moreover, to provide a quantitative velocity comparison, the experimental and numerical streamwise velocity profiles were extracted at three chordwise stations

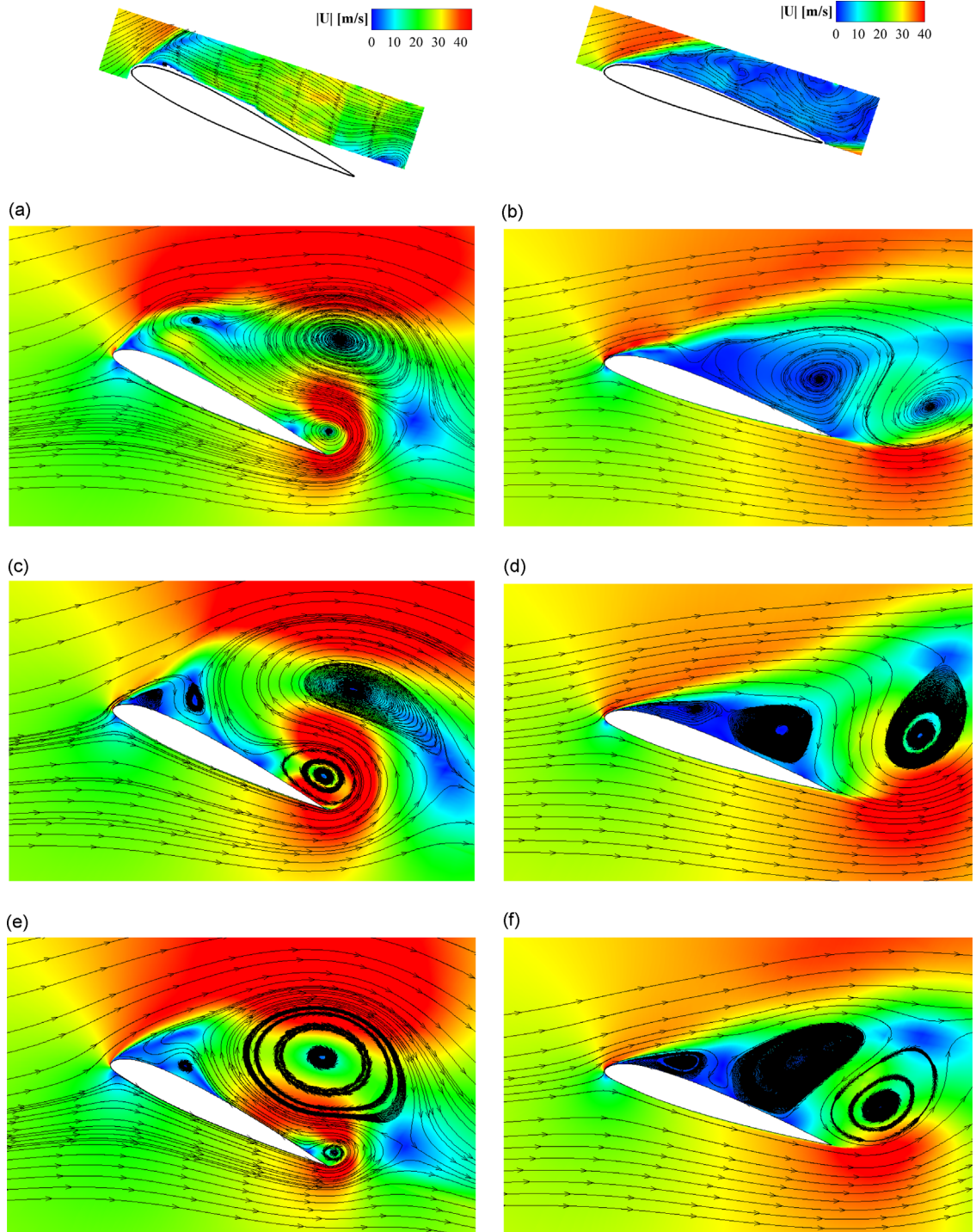


Fig. 17. Flow field comparison between experiments and CFD: streamlines superimposed on color maps of the velocity magnitude for $\alpha = 15^\circ + 10^\circ \sin(\omega t)$, $k=0.1$ ($Re=6 \times 10^5$ and $M=0.09$, Continued). (a) $\alpha = 25^\circ$ upstroke, Experiment, (b) $\alpha = 18^\circ$ downstroke, Experiment, (c) $\alpha = 25^\circ$ upstroke, CFD 3D – G4 720 TS, (d) $\alpha = 18^\circ$ downstroke, CFD 3D – G4 720 TS, (e) $\alpha = 25^\circ$ upstroke, CFD 2D – G1 720 TS, (f) $\alpha = 18^\circ$ downstroke, CFD 2D – G1 720 TS, (g) $\alpha = 25^\circ$ upstroke, CFD 2D – G2 720 TS and (h) $\alpha = 18^\circ$ downstroke, CFD 2D – G2 720 TS. (For interpretation of the references to color in this figure caption, the reader is referred to the web version of this article.)

corresponding to $x/c=0.25$, 0.5 and 0.75 and compared in Fig. 15 for the test case with $\alpha_m = 10^\circ$. The experimental velocity profiles plotted in Fig. 15 do not include the near-wall region of the attached boundary layer as laser reflections inhibit PIV measurements closer to the airfoil upper surface.

For the $\alpha_m = 10^\circ$ pitching cycle, at $\alpha = 18^\circ$ in upstroke, corresponding to a post-stall condition in the steady case, the flow field on the airfoil upper surface is fully attached, as shown in Fig. 13(a). As it is well known, the flow separation is delayed by a reduction in the adverse pressure gradient produced by the positive pitching rate (Leishman, 2006). For this condition the 2D and the 3D numerical models reproduce well the experimental flow field at midspan (see Fig. 13(c), (e) and (g)). A quantitative good agreement is shown also by the streamwise velocity profile comparison, as it can also be observed in Fig. 15(a).

For the present test case, the flow is attached for most of the upstroke motion. Separation starts only at the end of the upstroke motion, as illustrated in the flow field at $\alpha = 20^\circ$ in Fig. 13(b). The PIV flow field at $\alpha = 20^\circ$ shows a flow separation region which spans over more than half of the airfoil chord and which is characterised by the occurrence of small vortical structures, reproduced by the 3D simulation only (see Fig. 13(d)). The 2D simulations over both the considered grids show only a vortical structure at the trailing edge region (see Fig. 13(f) and (h)).

During the downstroke motion the flow on the airfoil upper surface is fully separated and it is characterised by the formation, displacement and shedding of strong vortices. At $\alpha = 18^\circ$ in downstroke the measured flow field presents a small vortex near the leading edge and a very large vortex at about half of the chord, as illustrated in Fig. 14(a). The aerodynamic features shown by the 3D numerical flow fields are qualitatively in good agreement with the experimental flow survey (see Fig. 14(c)), while the 2D numerical flow field shows a very similar behaviour characterised by two counter-rotating vortices near the trailing edge region (see Fig. 14(e) and (g)).

Also at $\alpha = 16^\circ$ in downstroke the experimental and the 3D numerical flow present a qualitative good agreement (Fig. 14(b) and (d)), while both the considered 2D numerical models are not capable to capture the experimental flow field in this condition, in particular close to the airfoil upper surface (see Fig. 14(f) and (h)). In fact, the 3D simulation reproduces the large region of reversed flow on the upper surface and a large vortex detaching the trailing edge, as shown in Fig. 14(b). The large recirculating flow region on the upper surface entraps air from the airfoil lower surface causing the formation of the counter-clockwise vortex located very close to the trailing edge (see Fig. 14(d)).

If separation occurs, the quantitative comparison between the experimental and numerical velocity profiles does not show an apparent trend as the curves are significantly dependent on the local position where the streamwise velocity profile is extracted, see Fig. 15(b)–(d).

Considering now the $\alpha_m = 15^\circ$ pitching cycle, at $\alpha = 23^\circ$ the flow field on the airfoil upper surface is dominated by the presence of the DSV structure. In particular, at this angle of attack the DSV reaches the airfoil midchord and spans over about the 50% of the airfoil upper surface, as it can be observed in Fig. 16(a). The simulated 3D flow field shows a vortical structure in the first half of the chord and another structure inside the separated flow region close to the trailing edge (see Fig. 16(c)). The simulated 2D flow field obtained over G1 grid shows a vortex structure with a similar chord-wise extent while the flow field obtained over G2 grid shows only the onset of flow separation at the trailing edge region that represents a preliminary stage prior to DSV formation (see Fig. 16(e) and (g)). The above may explain the higher delay of the 2D simulation over G2 grid in reproducing the DSV dynamics with respect to the experiment. A closer agreement with the experiment is observed for the 3D and 2D simulations over the same baseline mesh, as it was confirmed by the C_L curves comparison in Fig. 11(a).

By increasing the angle of attack, the DSV grows in size and intensity and moves downstream as shown in Fig. 16(b) for $\alpha = 24^\circ$. The growth of the DSV is well captured by the 3D and 2D simulations over the same baseline grid (see Fig. 16(d) and (f)), while the 2D approximation over G2 is believed to produce a delay in the formation of the DSV. Indeed, the 2D numerical results obtained over the finer grid at $\alpha = 24^\circ$ upstroke are closer to earlier experimental results at $\alpha = 23^\circ$ (see Fig. 16(h)).

At the maximum incidence of the oscillating cycle, $\alpha = 25^\circ$, the PIV flow field shows that the DSV has finally left the airfoil and that a small counter-clockwise vortical structure can be observed at the trailing edge (see Fig. 17(a)). The flow on the airfoil upper surface is fully separated and the reversed flow region spans over the entire airfoil chord within the measurement window area. Results from the 2D and 3D numerical models present some differences with respect to the experimental flow field, see Fig. 17(c), (e) and (g). Indeed, both 2D and 3D simulations deliver a large clockwise vortex very close to the airfoil upper surface, while at the trailing edge region the numerical flow fields show a counter-clockwise vortex in agreement to the PIV measurements.

During the downstroke motion the flow field on the airfoil upper surface is fully separated and characterised by the displacement of vortical structures on the airfoil upper surface, as it can be observed at $\alpha = 18^\circ$ in Fig. 17(b). For this angle of attack the two vortices shown by PIV measurements are well captured by the numerical models with a better agreement observed for the 3D model (see Fig. 17(d), (f) and (h)).

The comparison of the flow fields close to the airfoil upper surface shows an overall qualitative better agreement of the 3D simulation results with the experimental data, in particular for the test condition with $\alpha_m = 10^\circ$. Nevertheless, for the test condition with $\alpha_m = 15^\circ$ apparent discrepancies with the experimental flow fields were observed after the stall onset only, due to the complicated nature of the DSV dynamics. In general, it can be deduced from the flow fields analysis that after the stall onset three-dimensional effects characterise the aerodynamic behaviour of the airfoil under deep dynamic stall conditions and consequently a better representation in particular of the airfoil performance but also of the flow structures

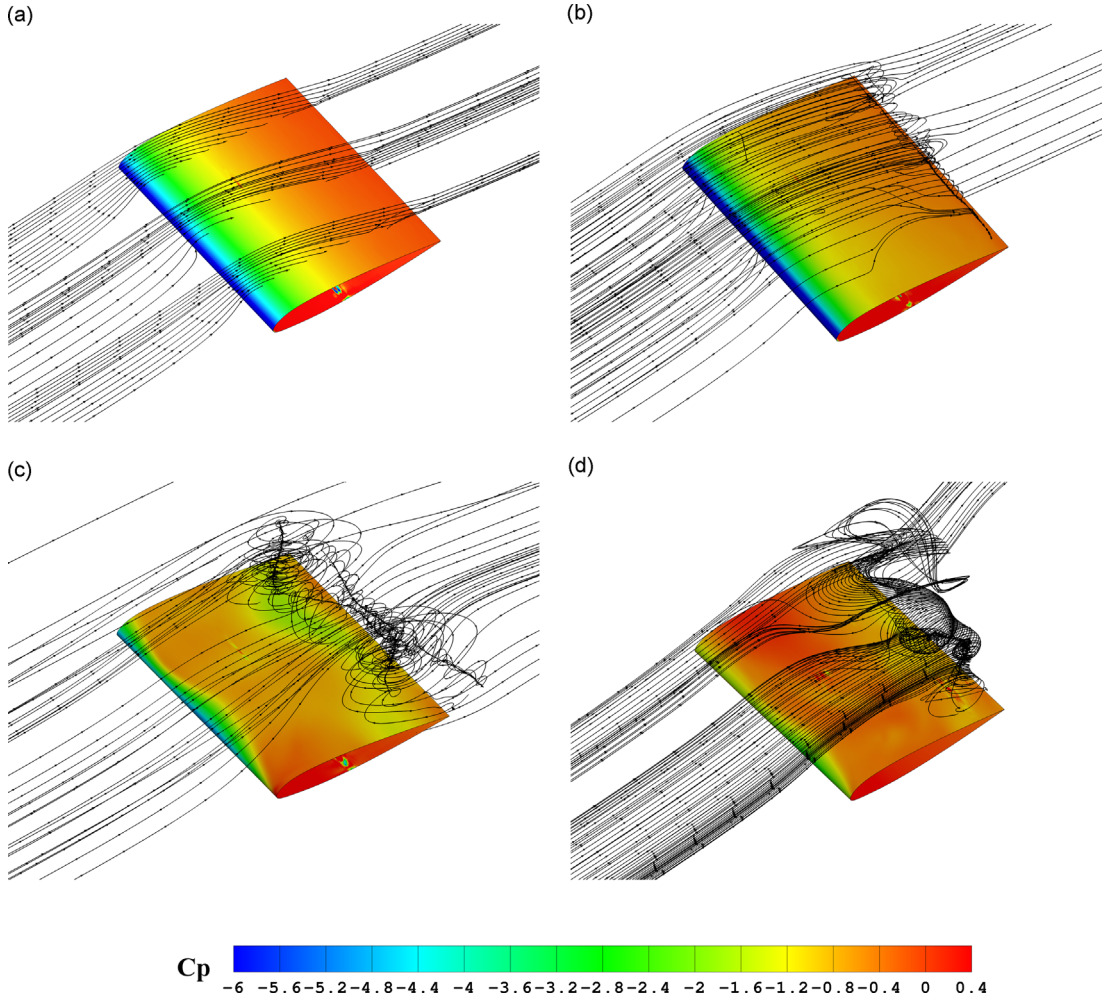


Fig. 18. 3D simulation results (G5 – 68 TS) illustrated by 3D streamline patterns and pressure coefficient distribution on the model surface: $\alpha = 10^\circ + 10^\circ \sin(\omega t)$, $k=0.1$, ($Re=6 \times 10^5$ and $M=0.09$). (a) $\alpha = 18^\circ$ upstroke, (b) $\alpha = 20^\circ$ upstroke, (c) $\alpha = 18^\circ$ downstroke and (d) $\alpha = 16^\circ$ downstroke.

can be achieved by a 3D numerical model (Klein et al., 2012; Wang et al., 2012). These 3D flow features occur mainly due to the intrinsic three-dimensional nature of dynamic stall phenomenon but they could also be in part related to the effects induced by the use of a finite-span model and by the wind tunnel side walls (see also Klein et al., 2012; Zanotti et al., 2014).

It is interesting to analyse the 3D simulations results to single out the operating conditions where these 3D effects are significant. Fig. 18 shows the 3D streamlines patterns around the model surface together with the pressure coefficient distribution on the model surface obtained with the 3D simulation over G5 for the test case with $\alpha_m = 10^\circ$. The results over a finer 3D grid enabled to achieve a better visualization of the 3D flow field. At $\alpha = 18^\circ$ and $\alpha = 20^\circ$ in upstroke the spanwise pressure distribution is quite uniform along the whole model span and strong three-dimensional effects are not appreciable (see Fig. 18(a) and (b)). At $\alpha = 18^\circ$ and $\alpha = 16^\circ$ during downstroke, 3D vortex structure shed downstream produces a strong alteration of pressure distribution on the whole model surface up to the tip (see Fig. 18(c) and (d)). The strong modification of the spanwise pressure and velocity field justifies the differences observed during downstroke motion between the 2D simulation and the experimental results.

5. Conclusions

Two-dimensional and three-dimensional CFD models for the NACA 23012 pitching airfoil were developed and compared to wind tunnel measurements of airloads and PIV flow surveys to achieve a deep insight about the suitability of numerical models for the simulation of airfoils deep dynamic stall experiments.

For the deep dynamic stall conditions tested, the 3D model reproduces better the measured airloads hysteresis with respect to the 2D model. In details, the comparison of the C_p distributions confirms a better agreement between experiments and the results of 3D simulations. Moreover, a qualitative better agreement with the overall experimental

flow fields is obtained from the 3D simulation results at some selected conditions for the test condition with $\alpha_m = 10^\circ$. In particular, after the stall onset the 2D model fails to reproduce the detailed flow physics and vortex dynamics exposed by the PIV surveys at the model midspan. For the test condition with $\alpha_m = 15^\circ$, discrepancies can be observed in the representation of the DSV dynamics with both the considered numerical models. The results presented in this work confirm that a three-dimensional representation can better reproduce the airfoil performance and the flow structures typical of this dynamic stall regime measured during experiments. This complex flow is characterised by the formation and shedding of strong vortex structures that move fast on the airfoil upper surface.

In fact, three-dimensional effects influence the flow field over the pitching airfoil in the deep dynamic stall regime. These three-dimensional effects on the flow field are of particular relevance in post-stall conditions and they are mainly due to the intrinsic three-dimensional nature of dynamic stall.

The good agreement between experimental and numerical results assesses the suitability of the numerical models for the characterisation of deep dynamic stall aerodynamics. In fact, it can be expected that a deep dynamic stall on an helicopter blade will show three-dimensional effects somehow different from those measured during wind tunnel experiments. However, up to now, experiments with this level of detail on a dynamic stall condition are not feasible on a rotor blade. As a consequence, the possibility to reach a good level of confidence in the numerical reproduction of wind tunnel experiments is expected to lead to the possibility to evaluate numerically the differences with the dynamic stall experienced on a rotor blade.

Acknowledgments

The authors would like to acknowledge Valentina Motta, Ph.D. candidate at Politecnico di Milano, for her support in the post-processing of the numerical results.

References

- Barbour, D., 2000. The ba-609 tiltrotor aircraft: a new way to fly in the 21st century. In: Proceeding of the Aircraft Symposium, vol. 38, pp. 805–816.
- Carr, L.W., McAlister, K.W., McCroskey, W.J., 1978. Dynamic Stall Experiments on the NACA 0012 Airfoil. NASA TP 1100.
- Catalano, F.M., Caixeta, P.R., 2004. Wind tunnel wall boundary layer control for 2d high lift wing testing. In: 24th International Congress of the Aeronautical Sciences (ICAS), Yokohama, Japan.
- Chandrasekhar, M., Martin, P., Tung, C., 2008. Compressible dynamic stall performance of a variable droop leading edge airfoil with a gurney flap. *Journal of the American Helicopter Society* 53, 18–25.
- Costes, M., Richiez, F., Le Pape, A., Gavriaux, R., 2011. Numerical investigation of three dimensional effects during dynamic stall. In: 37th European Rotorcraft Forum, Gallarate, VA, Italy.
- Coton, F., Galbraith, R.A.M., 1999. An experimental study of dynamic stall on a finite wing. *Aeronautical Journal* 103, 229–236.
- Desterac, D., 2011. Spurious far-field-boundary induced drag in two-dimensional flow simulations. *Journal of Aircraft* 48, 1444–1455.
- Drela, M., Youngren, H., 2001. XFOIL 6.94 User Guide. Cambridge, MA.
- Eliasson, P., 2002. Edge, a Navier-Stokes solver for unstructured grids. In: Proceedings of the Finite Volumes for Complex Applications III, vol. 1, pp. 527–534.
- Gardner, A., Richter, K., Mai, H., Altmikus, A.R.M., Klein, A., Rohardt, C.H., 2011. Experimental investigation of dynamic stall performance for the edi-m109 and edi-m112 airfoils. In: 37th European Rotorcraft Forum, Gallarate, VA, Italy.
- Gibertini, G., Auteri, F., Campanardi, G., Macchi, C., Zanotti, A., Stabellini, A., 2011. Wind-tunnel tests of a tilt-rotor aircraft. *Aeronautical Journal* 115, 315–322.
- Hellinsten, G., 2005. New advanced $k-\omega$ turbulence model for high-lift aerodynamics. *AIAA Journal* 43, 1857–1869.
- Joubert, G., Pape, A.L., Heine, B., Huberson, S., 2013. Deployable vortex generator dynamic stall alleviation through experimental and numerical investigation. *Journal of the American Helicopter Society* 50, 1–13.
- Klein, A., Lutz, T., Krämer, E., Richter, K., Gardner, A.D., Altmikus, A.R.M., 2012. Numerical comparison of dynamic stall for two-dimensional airfoils and an airfoil model in the dnw-twg. *Journal of the American Helicopter Society* 57, 1–13.
- Leishman, J.G., 1990. Dynamic stall experiments on the naca 23012 aerofoil. *Experiments in Fluids* 8, 49–58.
- Leishman, J.G., 2006. Principles of Helicopter Aerodynamics. Cambridge University Press, New York, NY.
- Leishman, J.G., 2007. The Helicopter: Thinking Forward, Looking Back. College Park Press, College Park.
- Martinat, G., Braza, M., Hoarau, Y., Harran, G., 2008. Turbulence modelling of the flow past a pitching naca 0012 airfoil at 10^5 and 10^6 Reynolds numbers. *Journal of Fluids and Structures* 24, 1294–1303.
- McCroskey, W.J., 1981. The Phenomenon of Dynamic Stall. NASA TM 81264.
- Nilifard, R., 2013. Assessment of Three-Dimensional Effects in Deep Dynamic Stall Over Oscillating Airfoils (Ph.D. thesis). Politecnico di Milano.
- Nishino, T., Shariff, K., 2010. Numerical study of wind-tunnel sidewall effects on circulation control airfoil flows. *AIAA Journal* 48, 2123–2132.
- Raffel, M., Gregorio, F.D., Sheng, W., Gibertini, G., Seraudie, A., de Groot, K., Schneider, O., 2011. On the generation of helicopter aerodynamic data base. *Aeronautical Journal* 115, 103–112.
- Raffel, M., Kompenhans, J., Stasicki, B., Brethauer, B., Meier, G.E.A., 1995a. Velocity measurement of compressible air flows utilizing a high-speed video camera. *Experiments in Fluids* 18, 204–206.
- Raffel, M., Kompenhans, J., Werner, P., 1995b. Investigation of the unsteady flow velocity field above an airfoil pitching under deep dynamic stall conditions. *Experiments in Fluids* 19, 103–111.
- Raffel, M., Willert, C., Kompenhans, J., 1998. Particle Image Velocimetry, A Practical Guide. Springer, Heidelberg.
- Richter, K., Pape, A.L., Knopp, T., Costes, M., Gleize, V., Gardner, A.D., 2011. Improved two-dimensional dynamic stall prediction with structured and hybrid numerical methods. *Journal of the American Helicopter Society* 56, 1–12.
- Spentzos, A., Barakos, G., Badcock, K., Richards, B., Werner, P., Schreck, S., Raffel, M., 2005. Investigation of three-dimensional dynamic stall using computational fluid dynamics. *AIAA Journal* 43, 1023–1033.
- Visbal, M.R., 2011. Numerical investigation of deep dynamic stall of a plunging airfoil. *AIAA Journal* 49, 2152–2170.
- Wallin, S., 2003. Engineering Turbulence Modeling for CFD with A Focus on Explicit Algebraic Reynolds Stress Models (Ph.D. thesis). Norsteds Tryckeri AB, Stockholm, Sweden.
- Wang, S., Ingham, D., Ma, L., Pourkashanian, M., Tao, Z., 2012. Turbulence modeling of deep dynamic stall at relatively low Reynolds number. *Journal of Fluids and Structures* 33, 191–209.
- Zanotti, A., 2012. Retreating Blade Dynamic Stall (Ph.D. thesis). Politecnico di Milano.

- Zanotti, A., Auteri, F., Campanardi, G., Gibertini, G., 2011. An experimental setup for the study of the retreating blade dynamic stall. In: 37th European Rotorcraft Forum, Gallarate, VA, Italy.
- Zanotti, A., Gibertini, G., 2013. Experimental investigation of the dynamic stall phenomenon on a naca 23012 oscillating aerofoil. *Proceedings of the Institution of Mechanical Engineers, Part G: Journal of Aerospace Engineering* 227, 1375–1388.
- Zanotti, A., Melone, S., Nilifard, R., D'Andrea, A., 2014. Experimental-numerical investigation of a pitching airfoil in deep dynamic stall. *Proceedings of the Institution of Mechanical Engineers, Part G: Journal of Aerospace Engineering* 228, 557–566, <http://dx.doi.org/10.1177/0954410013475954>.